Versatile inversion tool for phaseless optical diffraction: tomography

KEVIN D. UNGER, PATRICK C. CHAUMET, GUILLAUME MAIRE, ANNE SENTENAC,* AND KAMAL BELKEBIR

Institut Fresnel, Aix Marseille Univ, CNRS, Centrale Marseille, Marseille, France
Corresponding author: anne.sentenac@fresnel.fr

Estimating three-dimensional complex permittivity of a sample from the intensity recorded at the image plane of a microscope for various angles of illumination, as in optical Fourier ptychography microscopy, permits one to avoid the interferometric measurements of classical tomographic diffraction microscopes (TDMs). In this work, we present a general inversion scheme for processing intensities that can be applied to any microscope configuration (transmission or reflection, low or high numerical aperture), scattering regime (single or multiple scattering), or sample-holder geometries (with or without substrate). The inversion procedure is tested on a wide variety of synthetic experiments, and the reconstructions are compared to that of TDMs. In most cases, phaseless data yield the same result as complex data, thus paving the way toward a drastic simplification of TDM implementation.   © 2019 Optical Society of America

https://doi.org/10.1364/JOSAA.36.0000C1

1. INTRODUCTION

Optical diffraction tomography (ODT) [1], or tomographic diffraction microscopy (TDM) [2], is a quantitative imaging technique in which a sample is illuminated by a collimated laser beam under various angles of incidence, and an interferometric technique allows the recording of both the phase and intensity of the image fields. The permittivity of the sample is reconstructed numerically from the stack of complex fields using an inversion procedure. This approach proved to be particularly promising for obtaining three-dimensional images of marker-free samples with a resolution better than that of the best analogical microscopes and, in some cases, even beyond the diffraction limit [3,4].

Unfortunately, despite these achievements, TDM has still not been widely adopted as a reference imaging tool. In particular, the necessity to measure the phase of the image field, which complicates the setup and prevents the use of conventional microscopes, appears as a significant drawback. Thus, achieving the same performances with a simpler tomographic mounting in which only the intensity is recorded would enhance the interest for this computational imaging technique.

Phaseless diffraction tomography, in which the sample permittivity is reconstructed from intensity images recorded under various incident angles, has been recently popularized under the name of optical Fourier ptychography (OFP) [5–8]. Yet, up to now, it has been studied only in the case of transmission configuration with low numerical aperture (NA) objectives. These restrictions allow the use of approximate scalar forward models (such as the beam propagation method), which eases

significantly the reconstruction procedure. Qualitative 3D images of large samples with a moderate resolution (about a few micrometers) were obtained with this approach.

Now, to push forward the interest of phaseless tomography, its performances should be investigated with high NA objectives in both transmission and reflection geometries and for samples that potentially support multiple scattering. In these cases, the scalar approximate forward models on which the inversion schemes of OFP are presently based are not always valid. Hence, developing an inversion scheme that does not depend on a specific forward model and can be applied to any method for simulating the data would greatly enlarge the application domain of phaseless tomography.

In this work, we describe a versatile inversion procedure for phaseless diffraction tomography that provides reconstructions of the sample permittivity distribution in any imaging configuration. The key point of our inversion approach is that it does not depend on the model linking the recorded intensities to the sought permittivity distribution. Thus, it can be used with the approach best adapted to the samples: Born approximation in the weak scattering regime, beam propagation method in the forward scattering regime, or rigorous solver of Maxwell equations in the multiple scattering regime.

2. DERIVATION OF THE INVERSION SCHEME

We derive the inversion procedure for a very general monochromatic tomographic microscope in the rigorous framework of electromagnetism [9,10].

We introduce a reference geometry corresponding to the microscope *in the absence of the sample* (encompassing the lenses, glass slide, splitting cubes, sample holder, etc.), which is described by a spatially varying relative permittivity ε_{ref}. In the presence of the sample, the relative permittivity of the entire system becomes ε. Our aim is to estimate the sample contrast, $\chi = \varepsilon - \varepsilon_{ref}$. Hereafter, the latter is assumed to be equal to 0 outside a predefined bounded domain Ω. In addition, we assume that χ is scalar (isotropic media) but anisotropy can be accounted for without major modifications, as shown in Refs. [9,10].

The sample is lit by L different illuminations of wavenumber $k_0 = 2\pi/\lambda$ (which can be, but are not restricted to, collimated beams under various incident angles) that are generated by source distributions $\mathbf{Q}_l(\mathbf{r})$ for $l = 1, \dots, L$ (usually point sources at the backfocal plane of the objective for providing a collimated beam in Ω), and the field intensity is recorded at the observation points $\mathbf{o}_{m=1,\dots,M}$ of a domain Γ (which is generally the CCD camera).

We call $\mathbf{E}_l(\mathbf{r})$ the field generated by the l-th illumination in the microscope *in the presence of the sample*. It satisfies the equation

$$\nabla \times \nabla \times \mathbf{E}_l(\mathbf{r}) - k_0^2 \varepsilon_{ref}(\mathbf{r})\mathbf{E}_l(\mathbf{r}) = \mathbf{Q}_l(\mathbf{r}) + k_0^2 \chi(\mathbf{r})\mathbf{E}_l(\mathbf{r}), \quad (1)$$

with outgoing boundary condition. The total field $\mathbf{E}_l(\mathbf{r})$ can be written as the sum of a reference field (i.e., the field that would exist in the absence of the sample) generated by $\mathbf{Q}_l(\mathbf{r})$, $\mathbf{E}_l^{ref}(\mathbf{r})$, and a sample field (or scattered field) $\mathbf{E}_l^{diff}(\mathbf{r})$ generated by the induced source $k_0^2 \chi(\mathbf{r})\mathbf{E}_l(\mathbf{r})$.

We assume that we have a forward solver that is able to compute this field, at any point $\mathbf{o} \in \Gamma$ and for any χ in Ω. Then, the intensity recorded at the observation point $\mathbf{o}$ is modeled by $|\mathbf{E}_l(\mathbf{o})|^2$.

In addition, we assume that the forward solver is able to simulate the field at any point $\mathbf{r} \in \Omega$ that is radiated by any point source $\mathbf{Q}\delta(\mathbf{r} - \mathbf{o})$ located at the observation domain, $\mathbf{o} \in \Gamma$. This field, hereafter denoted by $\mathbf{E}(\mathbf{r}, \mathbf{o}, \mathbf{Q})$, is the solution of Eq. (1) with the source $\mathbf{Q}\delta(\mathbf{r} - \mathbf{o})$.

The inversion scheme consists of estimating iteratively χ in Ω so as to minimize the intensity-based diffractive tomography (IDT) cost functional,

$$\mathcal{F}(\chi) = \frac{\sum_{l=1}^{L} \|I_l^{mes} - |\mathbf{E}|^2\|_\Gamma^2}{\sum_{l=1}^{L} \|I_l^{mes}\|_\Gamma^2}, \quad (2)$$

where I^{mes} represents the actual intensities. The distance $\| \cdot \|_\Gamma$ is induced by the Hermitian product on Γ defined by $\langle f, g \rangle_\Gamma = \int_{\mathbf{o} \in \Gamma} f^*(\mathbf{o})g(\mathbf{o})d\mathbf{o}$, where * is the complex number conjugation. A similar distance will be defined for Ω.

For simplifying the notations, we introduce the residue $h_l(\mathbf{o}) = I_l^{mes}(\mathbf{o}) - |\mathbf{E}_l(\mathbf{o})|^2$ for any $\mathbf{o} \in \Gamma$ and introduce the normalizing factor $W_\Gamma = 1/\sum_l \|I_l^{mes}\|_\Gamma^2$.

The cost functional is minimized due to a classical gradient technique that updates iteratively χ with the relation

$$\chi_n = \chi_{n-1} + \alpha_n d_n, \quad (3)$$

where d_n is the Polak–Ribière descent

$$d_n = g_n + a_n d_{n-1}, \quad (4)$$

with

$$a_n = \frac{\langle g_n, g_n - g_{n-1} \rangle_\Omega}{\|g_{n-1}\|_\Omega^2}, \quad (5)$$

and g_n is the gradient at the n-th iteration of $\mathcal{F}$ with respect to χ, and α is real. Introducing Eq. (3) into Eq. (2), the cost functional is transformed into a polynomial with respect to α. Then, α is chosen so as to minimize this polynomial. The minimization can be performed analytically by finding the root of the polynomial, or it can be done numerically using a standard gradient algorithm. The main difficulty of the approach is to find the expression of the gradient, as $|\mathbf{E}_l|^2$ is related to χ in a non-explicit and non-linear form through Eq. (1). The most important result of this work lies in the rigorous expression of the gradient $g_n(\mathbf{r} \in \Omega)$, which is derived in Appendix A:

$$g_n(\mathbf{r})$$
$$= -4W_\Gamma \sum_{l=1}^{L} \int_{\mathbf{o} \in \Gamma} d\mathbf{o}[\mathbf{E}_{l,n-1}(\mathbf{r}, \mathbf{o}, h_{l,n-1}(\mathbf{o})\mathbf{E}_{l,n-1}^*(\mathbf{o})) \cdot \mathbf{E}_{l,n-1}(\mathbf{r})]^*. \quad (6)$$

It is seen that the gradient at the n-th iteration is the sum over the illuminations of the dot product between the field generated by the l-th illumination in Ω for the previous estimation of χ, $\mathbf{E}_{l,n-1}$, and the adjoint field created in Ω by a source distribution restricted to the observation domain Γ with amplitude, $h_{l,n-1}(\mathbf{o})\mathbf{E}_{l,n-1}(\mathbf{o})$, $\mathbf{o} \in \Gamma$.

The main interest of this gradient expression is that it does not depend on the model chosen for simulating the fields. Thus, if the samples are highly contrasted and support multiple scattering, the fields can be estimated with a rigorous Maxwell equation solver. On the contrary, if the samples are weakly scattering, the fields can be estimated with the first-order Born approximation or, if the forward scattering is dominant (as is assumed in most OFP applications), with the beam propagation method.

At this point, it is worth noting that a similar inversion scheme has been developed in Ref. [9] for inverting the data of imaging configurations that give access to the full-vectorial field $\mathbf{E}_l^{mes}$ (such as the tomographic microscope used in Ref. [11]). In this case, one estimates iteratively χ so as to minimize the vectorial-based diffractive tomography (VDT) cost functional,

$$\mathcal{F}_E(\chi) = \frac{\sum_{l=1}^{L} \|\mathbf{E}_l^{mes} - \mathbf{E}_l\|_\Gamma^2}{\sum_{l=1}^{L} \|\mathbf{E}_l^{mes}\|_\Gamma^2}, \quad (7)$$

with the same approach. The only difference lies in the gradient expression at the n-th iteration, which now reads

$$g_n^E(\mathbf{r}) = -4W_\Gamma \sum_{l=1}^{L} \int_{\mathbf{o} \in \Gamma} d\mathbf{o}[\mathbf{E}_{l,n-1}(\mathbf{r}, \mathbf{o}, \mathbf{h}_{l,n-1}^{E,*}(\mathbf{o})) \cdot \mathbf{E}_{l,n-1}(\mathbf{r})]^*. \quad (8)$$

In the field case, the amplitude of the source distribution restricted to Γ that generates the adjoint field is simply the vectorial residue $\mathbf{h}_{l,n-1}^E(\mathbf{o}) = \mathbf{E}_l^{mes}(\mathbf{o}) - \mathbf{E}_{l,n-1}(\mathbf{o})$. The two inversion schemes are thus very close to each other, which makes it easy to switch from one problem to the other.

In the following, we will study *in synthetic experiments* the performances of phaseless diffraction tomography for a wide

range of configurations, (microscopes in transmission, in reflection, with and without substrate) and several samples (finely structured in the transverse plane, extended along the optical axis, highly contrasted, with and without absorption) to point out the assets and limits of this imaging tool.

3. SYNTHETIC IMAGING EXPERIMENTS

A. Imaging Configuration

We consider a microscope made of an objective and a tube lens in a 4f mounting with NA, magnification M, and optical axis z oriented from the objective to the tube lens. The modeling of the microscope has been kept simple following [12], but more sophisticated point spread functions, taking into account, e.g., possible refractive mismatch [13,14] and aberrations, can be easily implemented by solely modifying the forward solver. We define the object space as the medium before the objective. For encompassing most imaging configurations, the sample in the object space is placed on a planar substrate (usually a glass slide) with interface placed at $z = 0$. The object space is described by its permittivity $\varepsilon_{\text{ref}}(\mathbf{z}) = \varepsilon_1$ for $z > 0$ and $\varepsilon_{\text{ref}}(\mathbf{z}) = \varepsilon_2$ for $z < 0$. The equality between ε_1 and ε_2 corresponds typically to cases where the samples are plunged in a solution whose permittivity matches that of the glass slide and are imaged with an oil-immersion objective.

The sample is illuminated by a monochromatic collimated beam under various incident angles. The latter is assimilated to a linearly polarized plane wave with varying transverse wavevector ($k_x^{\text{inc}}, k_y^{\text{inc}}$). In the reflection configuration, the incident beam is generated by a source at $z > 0$ and propagates towards the negative z, while in the transmission configuration, it is generated by a source at $z < 0$ and propagates towards positive z.

All the synthetic data are obtained using a rigorous solver of Maxwell equations [15] based on volume elements for calculating the field scattered by the sample and a rigorous modeling of the microscope following [12,16,17] for estimating the field at the image focal plane. The magnification of the microscope is assumed to be one, and the field at the image focal plane is calculated on a regular grid of 256×256 observation points to mimic the camera pixels. The simulation tool (including the Maxwell Solver and the microscope) is freely accessible at [18].

The discretization step used for the investigation domain Ω is the same as the one used for recording the data at the image focal plane. It depends on the sample refractive index n and is always smaller than $\lambda/(5n)$ to describe smoothly the electric field inside Ω. The synthetic data are deteriorated with additive white noise on the real and imaginary parts of the scattered field. For each illumination, the magnitude of the noise is chosen equal to κ times the difference between the maximum and the minimum of the values taken by the real part (resp. imaginary part) of the scattered field. Except in the last section, where a specific study with respect to noise has been conducted, the noise level, κ, is taken equal to 15% in all the numerical experiments.

For each numerical experiment, less than 10 different incident angles have been used for generating the data. Reconstructions using more incident angles (not shown) were

not significantly better. The important point is to choose the incident illuminations so as to ensure a good coverage of the accessible sample Fourier coefficients: in the single scattering regime, the scattered field in direction $\mathbf{k}$ obtained under incidence $\mathbf{k}_{\text{inc}}$ is proportional to the sample Fourier coefficient taken at $\mathbf{k} - \mathbf{k}_{\text{inc}}$. The angular step and span of the incident directions is determined by the size of the sample and the NA of the objective. Then, adding illuminations yields redundant information and is useful only to increase the signal-to-noise ratio.

All the iterative inversions are initialized with a constant $\chi = 0.001$ in the investigating domain Ω and are stopped when the cost functional reaches a plateau. To quantify the performance of the reconstruction at the last iteration, we introduce $\text{Err}(\chi)$ as the relative error $\frac{\|\chi - \chi^{\text{exact}}\|_\Omega^2}{\|\chi^{\text{exact}}\|_\Omega^2}$, where χ^{exact} is the actual permittivity contrast of the sample.

B. Investigating the Transverse Resolution of Phaseless Diffraction Tomography

One of the big achievements of TDM using complex field data is the significant improvement in transverse resolution compared to the equivalent conventional microscopes [11]. In this paragraph, we check if this gain is conserved with intensity data.

We consider a thin resin star (target A) made of 12 identical branches, with permittivity 2, height 160 nm, length 400 nm, and width 100 nm placed on a glass substrate that has already been used as a transverse resolution target in TDM studies [19]. The star is illuminated from the substrate, under total internal reflection, by six TM-polarized plane waves with wavelength 475 nm and wavevectors equally distributed along a 60° angle cone about the optical axis. The image field is obtained in the reflection configuration via an oil-objective (the oil index matching that of the glass slide) of NA = 0.95, discretized over a square grid of 256×256 pixels with step 50 nm. The object focal plane is taken at the air–glass interface, and the investigation domain Ω chosen for the inversion is a box of width 1900 nm and height 300 nm located on the glass slide. The simulations are performed with a rigorous solver of Maxwell equations.

We first study the brightfield configuration in which the specular reflection of the incident beam at the air–glass interface reaches the image plane. We thus record $|\mathbf{E}_l^{\text{ref}} + \mathbf{E}_l^{\text{diff}}|^2$. We compare the analogical brightfield image [Fig. 1(a)], obtained by summing the image intensities for all illuminations, to the numerical reconstruction, Fig. 1(d), obtained with our intensity inversion scheme in taking into account the specular reflection. As expected, the resolution of the latter is much better than that of the former. The stack of each intensity image conveys more information on the sample than the sum of these intensities.

We conduct a similar analysis in the darkfield configuration in which the specular reflection of the incident beam is filtered out and does not reach the image plane. We thus record $|\mathbf{E}_l^{\text{diff}}|^2$. The darkfield image, Fig. 1(b), obtained by summing the intensities, is compared to the numerical reconstruction, Fig. 1(e), obtained with our intensity inversion scheme without the specular reflection. The darkfield reconstruction (final relative
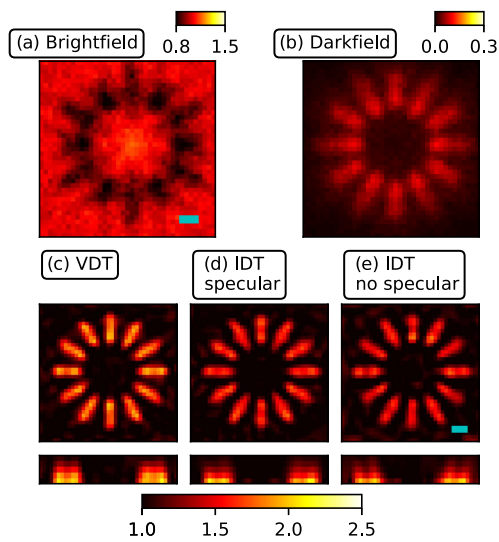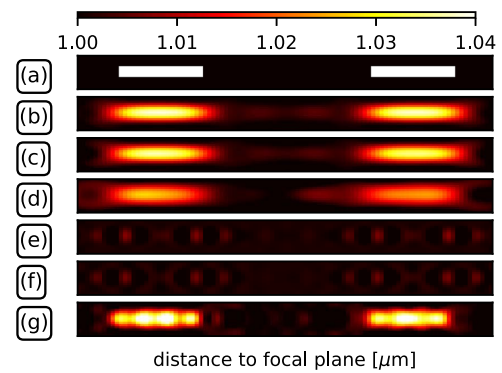
Fig. 1. (a) Brightfield image obtained by summing the image intensities for all illuminations. (b) Darkfield image obtained by filtering out the specular reflection of the incident beam and summing the image intensities for all illuminations. (c) Permittivity estimated of target A in reflection on a glass substrate with vectorial complex field data. (d) Permittivity estimated of target A in reflection on a glass substrate with intensity data. (e) Permittivity estimated of target A in reflection on a glass substrate with intensity data where the specular reflection of the incident beam has been filtered out. The green bar represents 200 nm. The final iteration is shown.

Fig. 2. (a) Theoretical permittivity of target B ($\varepsilon = 1.05$). Estimated permittivity of target B *in transmission*: (b) with complex vectorial data, (c) with intensity data, and (d) with intensity data where the specular reflection of the incident beam has been filtered out. Estimated permittivity of target B *in reflection*: (e) with complex vectorial data, (f) with intensity data in free space, and (g) with intensity data above a mirror. The final iteration is shown.

error Err(χ) = 79%), Fig. 1(e), remains better than the analogical darkfield image, Fig. 1(b), but is not as good as the brightfield reconstruction (final relative error Err(χ) = 62%), Fig. 1(d). This result does not come as a surprise, since the interference between the reference field and the sample field bring important information for the phase retrieval issue (as in line holography). Of course, the best reconstruction is still obtained with vectorial complex field data (final relative error Err(χ) = 57%); see Fig. 1(c). However, the difference between the reconstructions being relatively small, phaseless tomography appears as a very interesting option.

C. Investigating the Axial Resolution of Phaseless Diffractive Tomography

A key point of field tomography is its ability to reconstruct a 3D sample from 2D images that are recorded at a fixed plane for different angles of illumination. Under Born approximation, it can be shown that there is a one-to-one correspondence between the 2D stack of complex field data and the 3D Fourier transform of the sample restricted to the support of the optical transfer function of the microscope (which depends on the imaging configuration, reflection, or transmission and the NA) [20]. It is thus important to check whether this property is conserved with intensity data only. We consider a sample (target B) composed of two identical cuboids (edges along x and y axes 250 nm, edge along z axis 1 µm, $\varepsilon = 1.05$) separated by 2 µm along the optical axis. The cuboids are centered at 3.5 µm and 6.5 µm from the microscope focal plane; see Fig. 2(a). In a first numerical experiment, the sample is imaged in transmission with an air objective of NA = 0.95. It is illuminated by nine TM-polarized plane waves with illumination wavevectors equally distributed within a 30° angle cone about the optical axis, and the wavelength is $\lambda = 500$ nm. The discretization step at the image plane is 50 nm = $\lambda/10$. The simulations are performed with a rigorous solver of Maxwell equations.

In this configuration, the specular transmitted beam interferes with the sample field, and we observe that the 3D reconstruction obtained from the intensity data, Fig. 2(c), is very similar to that obtained from the full-vectorial field data, Fig. 2(b). If we artificially filter out the transmitted specular beams so that only the sample field reaches the image plane (darkfield configuration), the reconstruction is not as good; see Fig. 2(d), but still meaningful. As observed in Fig. 1, the interference with a specular field is useful, but its absence does not preclude totally the reconstruction.

In a second numerical experiment, the sample is imaged in the reflection configuration. The reconstructions obtained from the complex field and the intensity data, displayed in Figs. 2(e) and 2(f), look alike. The cubes are poorly retrieved, and only the interfaces can be located. This disappointing result does not come from a failure of the inversion algorithm. It is a direct illustration of the band-pass filtering of the reflection imaging system, which cuts the low spatial frequencies of the sample [10]. Without regularization, one cannot expect a better reconstruction in this case.

In a third numerical experiment, we aim at improving the imaging of the cubes by combining the transmission and reflection configurations. The two cubes are placed above a mirror that is placed at the focal plane of the microscope $z = 0$. By reflecting the illumination and the scattered field, the mirror sends both the transmitted and reflected fields toward the image plane [21]. As expected, the reconstruction of the cubes [Fig. 2(g)] is significantly improved compared to that obtained in transmission [Fig. 2(c)] or reflection [Fig. 2(f)] in agreement with the enlarged support of the optical transfer function [21]. Note that the data provided by other techniques specifically

developed for improving the resolution about the z axis, using sample rotation [22–24] or 4π configuration, e.g., could also be handled by the IDT algorithm.

D. Phaseless Tomography for Imaging Transparent and Absorbing Objects

An important limitation of the conventional brightfield microscopes [25] is that transparent (i.e., lossless) objects are invisible, while in darkfield configuration, they cannot be discriminated against lossy objects [26,27].

To be sensitive to these different contrasts, several imaging techniques, such as phase or differential interference contrast (DIC) microscopes have been developed. Now, if the recording of intensity images for various angles of incidence is sufficient for simulating a standard microscope, mimicking phase or DIC microscopy requires *a priori* the knowledge of the complex field at the image plane. The latter is obtained with the interferometric mounting of a tomographic diffraction microscope (TDM) and confers to this technique an interesting all-in-one multimodal imaging capability [28–31], but it is not accessible to our simpler configuration where phaseless data are recorded. The ability to obtain quantitative information on the complex permittivity of the sample from intensity data only is thus an important question.

In this paragraph, we consider a sample (target C) made of four cubes with different complex permittivities. The cubes of side 150 nm centered at the corners of a square of side 450 nm are placed (in air) at the object focal plane [Figs. 3(a) and 3(b)]. The cube permittivities, $\varepsilon = 1.1 + i0.1$, $\varepsilon = 1.0 + 1.0$, $\varepsilon = 2.0 + i0.5$, $\varepsilon = 1.5$, exhibit different levels of real and imaginary parts. Target C is illuminated by nine TM-polarized plane waves with polar angle 60°, azimuthal angle $q2\pi/9$ with $q = 0, \ldots, 8$ and $\lambda = 700$ nm. The discretization step at the image plane is 75 nm $= \lambda/9$. The simulations are performed with a rigorous solver of Maxwell equations. The reconstruction in the transmission configuration is given in Figs. 3(c) and 2(d). We observe that the variation on the real and imaginary levels of the permittivity of the cubes is
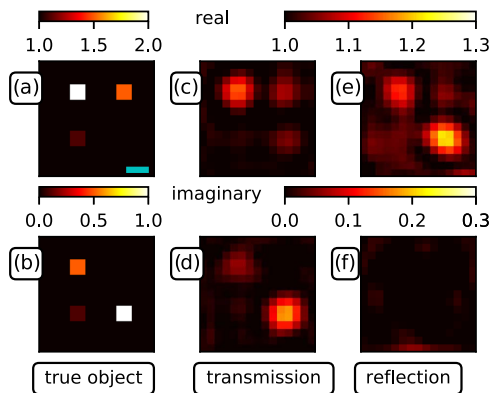
accurately retrieved. On the other hand, the reconstruction in the reflection configuration, in Figs. 3(e) and 2(f), does not permit one to distinguish the absorbing objects from the non-absorbing ones. This phenomenon was to be expected as, without the interference with a specular reflected or transmitted beam, a cube with a given imaginary contrast signs in the same way as a cube with the same contrast made real.

These synthetic experiments show that it is possible to retrieve the nature of the targets (phase or absorbing or mixed) by measuring the intensity as long as the scattered field interferes with a reference beam. An interesting perspective would be to investigate the ability of tomographic microscopy to image anisotropic samples. Our recent theoretical work on inversion scheme shows that this kind of extension would require only minor changes in the reconstruction algorithm [9].

E. Phaseless Tomography in the Multiple Scattering Regime

Up to now, we have considered small targets or targets with low contrast for which the single scattering approximation (or Born approximation) is valid. In this paragraph, we investigate the performance of the intensity inversion scheme for a target that supports multiple scattering. The sample (target D) is made of two identical spheres in contact of diameter 250 nm ($\varepsilon = 2.05$ aligned along the x axis, Fig. 4. The contact point is placed at the object focal plane. The spheres are embedded in air and illuminated by nine TM-polarized plane waves with wavelength 450 nm and wavevectors regularly chosen along a 60° angle cone with the optical axis. The target is imaged in
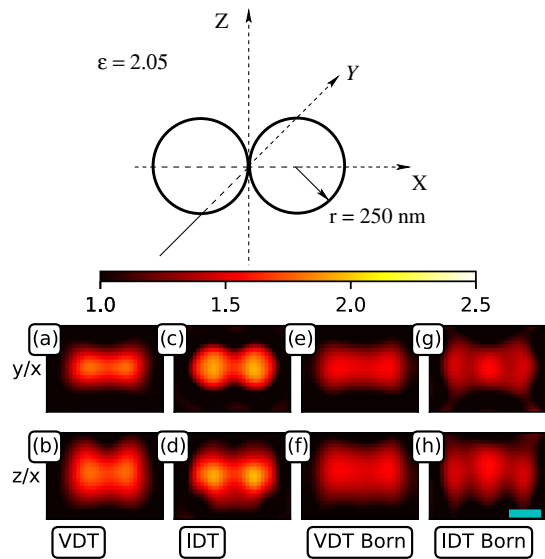
Fig. 4. Permittivity estimated of target D in transmission with complex vectorial data with rigorous computation of the field: (a) transversal plane and (b) axial plane. Permittivity estimated of target D in transmission with intensity data with rigorous computation of the field: (c) transversal plane and (d) axial plane. Permittivity estimated of target D in transmission with complex vectorial data with Born approximation: (e) transversal plane and (f) axial plane. Permittivity estimated of target D in transmission with intensity data with Born approximation: (g) transversal plane and (h) axial plane. The green bar measures 200 nm. The final iteration is shown.

Fig. 3. Theoretical permittivity of target C: (a) real part and (b) imaginary part. Estimated permittivity of target C with intensity data *in transmission*: (c) real part and (d) imaginary part. Estimated permittivity of target C with intensity data *in reflection*: (e) real part and (f) imaginary part. The final iteration is shown. The green bar measures 200 nm.

transmission configuration with NA = 0.95, and the intensities are recorded at the image plane with a discretization step of 25 nm, i.e., $\lambda/18$.

We plot in Fig. 4 the reconstructions obtained from the intensities and the full vectorial field using either a rigorous solver of Maxwell equations for calculating the gradients or the Born approximation. As expected, a more accurate reconstruction is obtained when the gradients are estimated rigorously, as under the Born approximation, the inversion scheme fails to retrieve the two spheres; see Figs. 4(e)–4(h). With the rigorous solver, both spheres are retrieved. The reconstructions obtained from the intensities and the full vectorial field with rigorous computation of the field are close to final relative errors Err(χ), equal to 45% and 41%, respectively.
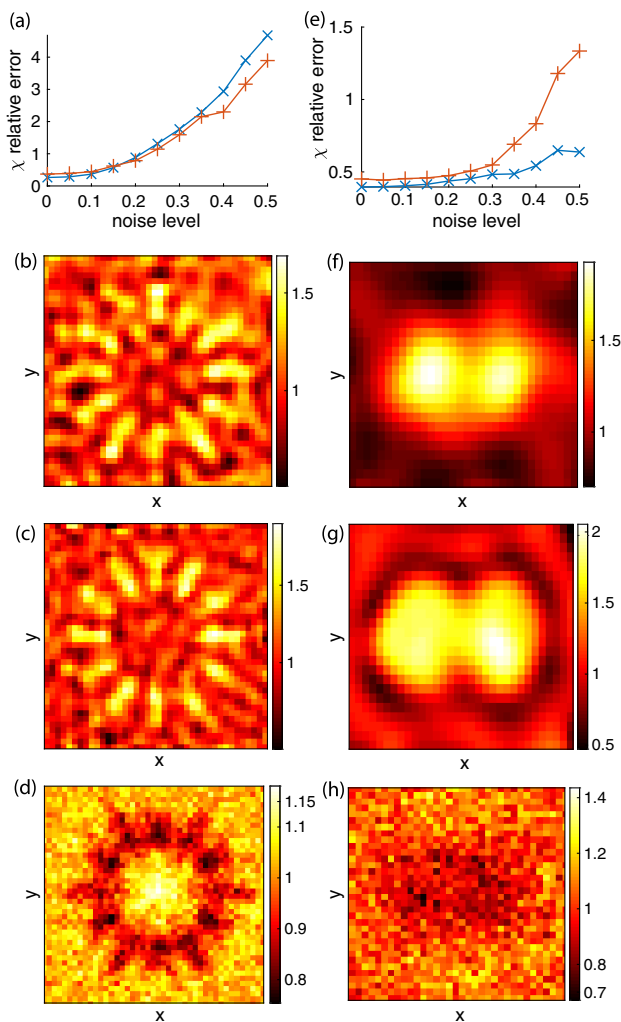
Fig. 5. Robustness of the reconstruction of target A (left column) and target D (right column) with respect to noise. Top row: evolution of the reconstruction error Err(χ) with respect to the noise level κ (red "+" curve: intensity data; blue "×" curve: complex vectorial data). Second row: final reconstructions obtained from vectorial field data with $\kappa = 25\%$. Third row: final reconstructions obtained from intensity data with $\kappa = 25\%$. Bottom row: images obtained by summing the noisy intensities. The numerical reconstructions are significantly better than the "analogical" images.

F. Robustness of the Reconstructions with Respect to Noise

In this paragraph, we investigate the performance of the reconstruction algorithms when the noise is increased. We consider two targets, the resin star (target A), which exhibits high spatial frequency features, and the bisphere (target D), which has a more regular shape but supports multiple scattering, in the same configurations as those in Sections B and E.

We increase the noise level κ from 0% to 50% and plot the reconstruction relative error Err(χ) in Fig. 5. We observe without surprise that Err(χ) increases with the noise level but that the reconstructions are always significantly better than the standard microscopy images obtained by summing all the intensities. In addition, the deterioration of the intensity-based reconstruction remains comparable to that of the field-based reconstruction. Thus, it is expected that the sensitivity to noise of the IDT algorithm be similar to that of VDT, which has been shown to be able to handle experimental data with more than 80% of noise [4].

4. CONCLUSION

In conclusion, we have presented an inversion scheme able to reconstruct the complex permittivity of a sample from intensity images obtained under various incident angles. Our algorithm can be adapted to any model used for simulating the images and to any microscope configuration (in reflection or transmission with low or high NA). We have investigated the phaseless tomography performances on four main issues—transverse super-resolution, three-dimensional reconstruction (in reflection and transmission), contrast detection, and multiple scattering regime—and compared them to that of tomography using complex field data. We have found that, in most cases, phaseless tomography exhibited the same gain in resolution and contrast as field tomography. It is thus a very interesting option for popularizing computational tomographic microscopy, as it requires minor changes in the microscope setup.

APPENDIX A: DERIVATION OF THE GRADIENT

In Appendix A, we detail the derivation of the gradient.

A. Linearization of the Scattering Model: Fréchet Derivative

Hereafter, $\mathbf{E}^\chi$ denotes the field existing in the medium of contrast χ for a given illumination (the subscript l is omitted). It is non-linearly linked to χ through a differential equation, given by Eq. (1). The calculation of the gradient of the cost functional requires to linearize the model linking the field $\mathbf{E}^\chi$ to χ. We thus introduce the Fréchet derivative, which is the unique linear operator $\overline{\mathbf{D}}_\chi$, which gives a linear variation of the field with respect to a small variation of the contrast $\delta\chi$:

$$\mathbf{E}^{\chi+\delta\chi} = \mathbf{E}^\chi + \overline{\mathbf{D}}_\chi \delta\chi + o(\delta\chi). \tag{A1}$$

To estimate the Fréchet derivative, we rewrite the differential equation satisfied by $\mathbf{E}^\chi$, Eq. (1), into the integral equation

$$\mathbf{E}^\chi(\mathbf{r}) = \mathbf{E}^{\mathrm{ref}}(\mathbf{r}) + \int_{\mathbf{r}'\in\Omega} d\mathbf{r}'\overline{\mathbf{G}}(\mathbf{r},\mathbf{r}')\chi(\mathbf{r}')\mathbf{E}^\chi(\mathbf{r}'), \tag{A2}$$

where $\overline{\mathbf{G}}(\mathbf{r}, \mathbf{r}')\chi(\mathbf{r}')\mathbf{E}^\chi(\mathbf{r}')$ is the field existing at $\mathbf{r}$ in the microscope *without the sample* radiated by a source $\chi(\mathbf{r}')\mathbf{E}^\chi(\mathbf{r}')$ placed at $\mathbf{r}'$. If we modify χ by a small perturbation $\delta\chi$, we have

$$\mathbf{E}^{\chi+\delta\chi}(\mathbf{r}) = \mathbf{E}^{\mathrm{ref}}(\mathbf{r}) + \int_{\mathbf{r}'\in\Omega} d\mathbf{r}'\overline{\mathbf{G}}(\mathbf{r},\mathbf{r}')(\chi+\delta\chi)(\mathbf{r}')\mathbf{E}^{\chi+\delta\chi}(\mathbf{r}').$$

$$\text{(A3)}$$

Neglecting the terms of second order in $\delta\chi$ yields

$$\mathbf{E}^{\chi+\delta\chi}(\mathbf{r}) = \mathbf{E}^\chi(\mathbf{r}) + \int_{\mathbf{r}'\in\Omega} d\mathbf{r}'\overline{\mathbf{G}}(\mathbf{r},\mathbf{r}')\delta\chi(\mathbf{r}')\mathbf{E}^\chi(\mathbf{r}') + o(\delta\chi).$$

$$\text{(A4)}$$

Since $\mathbf{E}^{\mathrm{ref}}(\mathbf{o})$ does not depend on the media, we have for a dipole $\mathbf{p}$ located at an observation position $\mathbf{o}$

$$\mathbf{p}\cdot\delta\mathbf{E}^\chi(\mathbf{o}) = \mathbf{p}\cdot[\mathbf{E}^{\chi+\delta\chi} - \mathbf{E}^\chi](\mathbf{o})$$

$$= \int_{\mathbf{r}'\in\Omega} d\mathbf{r}'\mathbf{p}\cdot\overline{\mathbf{G}}(\mathbf{o},\mathbf{r}')[\delta\chi(\mathbf{r}')\mathbf{E}^\chi(\mathbf{r}')]. \quad\text{(A5)}$$

Now, the Lorentz reciprocity theorem states that if the two sources $\mathbf{u}$ and $\mathbf{v}$ are located at positions $\mathbf{r}$ and $\mathbf{r}'$, respectively, we have $\mathbf{u}\cdot[\overline{\mathbf{G}}(\mathbf{r},\mathbf{r}')\mathbf{v}] = \mathbf{v}\cdot[\overline{\mathbf{G}}(\mathbf{r}',\mathbf{r})\mathbf{u}]$. We apply the reciprocity theorem on Eq. (A5) and obtain

$$\mathbf{p}\cdot\delta\mathbf{E}^\chi(\mathbf{o}) = \int_{\mathbf{r}'\in\Omega} d\mathbf{r}'[\delta\chi(\mathbf{r}')\mathbf{E}^\chi(\mathbf{r}')]\cdot\overline{\mathbf{G}}(\mathbf{r}',\mathbf{o})\mathbf{p}. \quad\text{(A6)}$$

Introducing $\mathbf{E}^\chi(\mathbf{r}',\mathbf{o},\mathbf{p}) = \overline{\mathbf{G}}(\mathbf{r}',\mathbf{o})\mathbf{p}$, the field in the medium with contrast χ radiated by a source $\mathbf{p}$ located at $\mathbf{o}$, we obtain

$$\mathbf{p}\cdot\delta\mathbf{E}^\chi(\mathbf{o}) = \int_{\mathbf{r}'\in\Omega} d\mathbf{r}'[\mathbf{E}^\chi(\mathbf{r}',\mathbf{o},\mathbf{p})\cdot\mathbf{E}^\chi](\mathbf{r}')\delta\chi(\mathbf{r}'). \quad\text{(A7)}$$

By identification with Eq. (A1), we have

$$\mathbf{p}\cdot\overline{\mathbf{D}}(\mathbf{o},\mathbf{r}) = \mathbf{E}^\chi(\mathbf{r})\cdot\mathbf{E}^\chi(\mathbf{r},\mathbf{o},\mathbf{p}). \quad\text{(A8)}$$

B. Detailed Derivation of the Gradient

Once the Fréchet operator is known, we introduce the gradient $\mathbf{g}$ of the cost functional $\mathcal{F}(\chi)$ with respect to χ as

$$\mathcal{F}(\chi+\delta\chi) = \mathcal{F}(\chi) + \mathrm{Re}\langle\mathbf{g},\delta\chi\rangle_\Omega + o(\delta\chi). \quad\text{(A9)}$$

Now, let us differentiate $\mathcal{F}$ with respect to χ:

$$\mathcal{F}(\chi+\delta\chi) = W_\Gamma\sum_l\|I_l^{\mathrm{mes}} - (\mathbf{E}_l^\chi + \overline{\mathbf{D}}_l\delta\chi)^*\cdot(\mathbf{E}_l^\chi + \overline{\mathbf{D}}_l\delta\chi)\|_\Gamma^2,$$

$$= W_\Gamma\sum_l\|h_l - 2\,\mathrm{Re}(\mathbf{E}_l^{\chi*}\cdot(\overline{\mathbf{D}}_l\delta\chi)) + o(\delta\chi)\|_\Gamma^2,$$

$$= \mathcal{F}(\chi) - 2W_\Gamma\sum_l\mathrm{Re}\langle h_l, 2\,\mathrm{Re}(\mathbf{E}_l^{\chi*}\cdot(\overline{\mathbf{D}}_l\delta\chi))\rangle_\Gamma$$

$$+ o(\delta\chi), \quad\text{(A10)}$$

and since h is real,

$$\mathcal{F}(\chi+\delta\chi) = \mathcal{F}(\chi) - 4W_\Gamma\sum_l\mathrm{Re}\langle h_l, \mathbf{E}_l^{\chi*}\cdot(\overline{\mathbf{D}}_l\delta\chi)\rangle_\Gamma + o(\delta\chi).$$

$$\text{(A11)}$$

We have

$$\langle h_l\mathbf{E}_l^{\chi*}\cdot(\overline{\mathbf{D}}_l\delta\chi)\rangle_\Gamma = \int_\Gamma d\mathbf{r}'h_l(\mathbf{r}')\mathbf{E}_l^{\chi*}\cdot[\overline{\mathbf{D}}\delta\chi](\mathbf{r}'),$$

$$= \int_\Gamma d\mathbf{r}'\int_\Omega d\mathbf{r}h_l(\mathbf{r}')\mathbf{E}_l^{\chi*}(\mathbf{r}')\cdot\overline{\mathbf{D}}_l(\mathbf{r}',\mathbf{r})\delta\chi(\mathbf{r}),$$

$$= \int_\Omega d\mathbf{r}\delta\chi(\mathbf{r})\left(\int_\Gamma d\mathbf{r}'h(\mathbf{r}')\mathbf{E}_l^{\chi*}(\mathbf{r}')\cdot\overline{\mathbf{D}}_l(\mathbf{r}',\mathbf{r})\right),$$

$$= \int_\Omega d\mathbf{r}\delta\chi(\mathbf{r})\left[-\frac{1}{4W_\Gamma}\mathbf{g}_{\chi l}^*(\mathbf{r})\right]. \quad\text{(A12)}$$

Finally,

$$\mathbf{g}(\mathbf{r}) = -4W_\Gamma\sum_l\mathbf{g}_l(\mathbf{r}),$$

$$= -4W_\Gamma\sum_l\left(\int_\Gamma d\mathbf{r}'h(\mathbf{r}')\mathbf{E}_l^{\chi*}(\mathbf{r}')\cdot\overline{\mathbf{D}}_l(\mathbf{r}',\mathbf{r})\right)^*. \quad\text{(A13)}$$

APPENDIX B: HOW α_n AND β_n ARE DETERMINED

In Appendix B, we detail the choice of the scalars α_n and β_n in the iterative intensity and field inversion procedures.

A. Inversion from Intensity Data

The cost functional reads

$$\mathcal{F}(\chi_+\delta\chi) \approx W_\Gamma\sum_l\|h_l - 2\,\mathrm{Re}(\mathbf{E}_l^{\chi*}\cdot\overline{\mathbf{D}}_l\delta\chi) - |\overline{\mathbf{D}}_l\delta\chi|^2\|_\Gamma^2.$$

$$\text{(B1)}$$

If we set

$$P_l^0(\mathbf{r}) = h_l(\mathbf{r}), \quad\text{(B2)}$$

$$P_l^1(\mathbf{r}) = 2\,\mathrm{Re}(\mathbf{E}_l^{\chi*}\cdot\overline{\mathbf{D}}_l\delta\chi)(\mathbf{r}), \quad\text{(B3)}$$

$$P_l^2(\mathbf{r}) = |\overline{\mathbf{D}}_l\delta\chi|^2(\mathbf{r}), \quad\text{(B4)}$$

$$P_l^{00} = \|P_l^0\|_\Gamma^2, \quad\text{(B5)}$$

$$P_l^{11} = \|P_l^1\|_\Gamma^2, \quad\text{(B6)}$$

$$P_l^{22} = \|P_l^2\|_\Gamma^2, \quad\text{(B7)}$$

$$P_l^{01} = \langle P_l^0, P_l^1\rangle_\Gamma, \quad\text{(B8)}$$

$$P_l^{02} = \langle P_l^0, P_l^2\rangle_\Gamma, \quad\text{(B9)}$$

$$P_l^{12} = \langle P_l^1, P_l^2\rangle_\Gamma, \quad\text{(B10)}$$

we have

$$\mathcal{F}(\chi+\delta\chi) \approx W_\Gamma\sum_l(P_l^{00} + P_l^{11} + P_l^{22}$$

$$- 2P_l^{01} - 2P_l^{02} + 2P_l^{12}). \quad\text{(B11)}$$

At iteration $n+1$, $\chi_{n+1} = \chi_n + \delta\chi$. We choose $\delta\chi = \alpha_n d_n$, and by redefining the coefficients introduced in Eqs. (B2) to (B10), we transform the cost functional into a polynomial in α_n:

$$\mathcal{F}(\alpha_n) = W_\Gamma \sum_l (P_l^{00} + \alpha_n^2 P_l^{11} + \alpha_n^4 P_l^{22}$$
$$- 2\alpha_n P_l^{01} - 2\alpha_n^2 P_l^{02} + 2\alpha_n^3 P_l^{12}). \quad \textbf{(B12)}$$

The coefficient α_n is determined by minimizing the polynomial $\mathcal{F}(\alpha_n)$.

B. Inversion of Complex-Field Data

Setting $\delta\chi = \beta_n d_n$, the cost functional reads

$$\mathcal{Q}(\chi + \delta\chi) \approx W_\Gamma \sum_l (\|\mathbf{v}_l\|_\Gamma^2 - 2\operatorname{Re}\langle \mathbf{E}_l^d, \overline{\mathbf{D}}_l \delta\chi \rangle_\Gamma + \|\overline{\mathbf{D}}_l \delta\chi\|_\Gamma^2),$$

$$\approx W_\Gamma \sum_l (\|\mathbf{v}_l\|_\Gamma^2 - 2\beta_n \operatorname{Re}\langle \mathbf{E}_l^d, \overline{\mathbf{D}}_l \mathbf{t}_\chi \rangle_\Gamma + \beta_n^2 \|\overline{\mathbf{D}}_l \mathbf{t}_\chi\|_\Gamma^2).$$

$$\textbf{(B13)}$$

The function $\mathcal{Q}(\beta_n)$ is a parabola, and its minimum is at the abscissa

$$\beta_n = W_\Gamma \frac{\sum_l \operatorname{Re}\langle \mathbf{E}_l^d, \overline{\mathbf{D}}_l \mathbf{t}_{\chi l} \rangle_\Gamma}{\sum_l \|\overline{\mathbf{D}}_l \mathbf{t}_{\chi n}\|_\Gamma^2}. \quad \textbf{(B14)}$$

To speed up the computations, the coefficients of the polynomial (see Appendix A) are computed with a Born approximation on the adjoint field, i.e., that $\mathbf{u}(\mathbf{o}) \cdot \overline{\mathbf{D}}(\mathbf{o}, \mathbf{r}) \approx [\mathbf{E}^{\mathbf{u}(\mathbf{o})} \cdot \mathbf{E}](\mathbf{r})$, where $\mathbf{E}^{\mathbf{u}(\mathbf{o})}$ is the field in the absence of the sample with a dipole $\mathbf{u}(\mathbf{o})$ at observation $\mathbf{o}$.

REFERENCES

1. V. Lauer, "New approach to optical diffraction tomography yielding a vector equation of diffraction tomography and a novel tomographic microscope," J. Microsc. **205**, 165–176 (2002).
2. B. Simon, M. Debailleul, V. Georges, V. Lauer, and O. Haeberlé, "Tomographic diffractive microscopy of transparent samples," Eur. Phys. J. **44**, 29–35 (2008).
3. Y. Park, C. Depeursinge, and G. Popescu, "Quantitative phase imaging in biomedicine," Nat. Photonics **12**, 578–589 (2018).
4. T. Zhang, C. Godavarthi, P. C. Chaumet, G. Maire, H. Giovannini, A. Talneau, M. Allain, K. Belkebir, and A. Sentenac, "Far-field diffraction microscopy at λ/10 resolution," Optica **3**, 609–612 (2016).
5. L. Tian and L. Waller, "3d intensity and phase imaging from light field measurements in an led array microscope," Optica **2**, 104–111 (2015).
6. T.-A. Pham, E. Soubies, A. Goy, J. Lim, F. Soulez, D. Psaltis, and M. Unser, "Versatile reconstruction framework for diffraction tomography with intensity measurements and multiple scattering," Opt. Express **26**, 2749–2763 (2018).
7. A. M. Maiden, M. J. Humphry, and J. M. Rodenburg, "Ptychographic transmission microscopy in three dimensions using a multi-slice approach," J. Opt. Soc. Am. A **29**, 1606–1614 (2012).
8. G. Zheng, R. Horstmeyer, and C. Yang, "Wide-field, high-resolution Fourier ptychographic microscopy," Nat. Photonics **7**, 739–745 (2013).
9. K. Unger, T. Zhang, P. C. Chaumet, A. Sentenac, and K. Belkebir, "Linearized inversion methods for three-dimensional electromagnetic imaging in the multiple scattering regime," J. Mod. Opt. **65**, 1787–1792 (2018).
10. A. Sentenac and J. Mertz, "Unified description of three-dimensional optical diffraction microscopy: from transmission microscopy to optical coherence tomography: tutorial," J. Opt. Soc. Am. A **35**, 748–754 (2018).
11. T. Zhang, Y. Ruan, G. Maire, D. Sentenac, A. Talneau, K. Belkebir, P. C. Chaumet, and A. Sentenac, "Full-polarized tomographic diffraction microscopy achieves a resolution about one-fourth of the wavelength," Phys. Rev. Lett. **111**, 243904 (2013).
12. S. Khadir, P. C. Chaumet, G. Baffou, and A. Sentenac, "Quantitative model of the image of a radiating dipole through a microscope," J. Opt. Soc. Am. A **36**, 478–484 (2019).
13. M. J. Nasse and J. C. Woehl, "Realistic modeling of the illumination point spread function in confocal scanning optical microscopy," J. Opt. Soc. Am. A **27**, 295–302 (2010).
14. O. Haeberlé, "Focusing of light through a stratified medium: a practical approach for computing microscope point spread functions. Part ii: confocal and multiphoton microscopy," Opt. Commun. **235**, 1–10 (2004).
15. P. C. Chaumet, A. Sentenac, and A. Rahmani, "Coupled dipole method for scatterers with large permittivity," Phys. Rev. E **70**, 036606 (2004).
16. L. Novotny, D. W. Pohl, and P. Regli, "Light propagation through nanometer-sized structures: the two-dimensional-aperture scanning near-field optical microscope," J. Opt. Soc. Am. A **11**, 1768–1779 (1994).
17. B. Richards, E. Wolf, and D. Gabor, "Electromagnetic diffraction in optical systems. ii. Structure of the image field in an aplanatic system," Proc. R. Soc. London, Ser. A **253**, 358–379 (1959).
18. P. C. Chaumet, A. Sentenac, and D. Sentenac, "The computations were done using the free software IFDDA," https://github.com/pchaumet/IF-DDA.
19. C. Godavarthi, T. Zhang, G. Maire, P. C. Chaumet, H. Giovannini, A. Talneau, K. Belkebir, and A. Sentenac, "Superresolution with full-polarized tomographic diffractive microscopy," J. Opt. Soc. Am. A **32**, 287–292 (2015).
20. O. Haeberlé, K. Belkebir, H. Giovaninni, and A. Sentenac, "Tomographic diffractive microscopy: basics, techniques and perspectives," J. Mod. Opt. **57**, 686–699 (2010).
21. E. Mudry, P. C. Chaumet, K. Belkebir, G. Maire, and A. Sentenac, "Mirror-assisted tomographic diffractive microscopy with isotropic resolution," Opt. Lett. **35**, 1857–1859 (2010).
22. S. Vertu, J.-J. Delaunay, I. Yamada, and O. Haeberlé, "Diffraction microtomography with sample rotation: influence of a missing apple core in the recorded frequency space," Central Eur. J. Phys. **7**, 22–31 (2009).
23. B. Vinoth, X.-J. Lai, Y.-C. Lin, H.-Y. Tu, and C.-J. Cheng, "Integrated dual-tomography for refractive index analysis of free-floating single living cell with isotropic superresolution," Sci. Rep. **8**, 5943 (2018).
24. B. Simon, M. Debailleul, M. Houkal, C. Ecoffet, J. Bailleul, J. Lambert, A. Spangenberg, H. Liu, O. Soppera, and O. Haeberlé, "Tomographic diffractive microscopy with isotropic resolution," Optica **4**, 460 (2017).
25. N. Streibl, "Three-dimensional imaging by a microscope," J. Opt. Soc. Am. A **2**, 121–127 (1985).
26. M. Born and E. Wolf, *Principles of Optics* (Pergamon, 1959).
27. M. W. Davidson and M. Abramowitz, *Optical Microscopy* (American Cancer Society, 2002).
28. J. Lobera and J. M. Coupland, "Contrast enhancing techniques in digital holographic microscopy," Meas. Sci. Technol. **19**, 025501 (2008).
29. L. Miccio, A. Finizio, R. Puglisi, D. Balduzzi, A. Galli, and P. Ferraro, "Dynamic dic by digital holography microscopy for enhancing phase-contrast visualization," Biomed. Opt. Express **2**, 331–344 (2011).
30. J. Bailleul, B. Simon, M. Debailleul, and O. Haeberlé, "An introduction to tomographic diffractive microscopy," in *Micro- and Nanophotonic Technologies*, P. Meyrueis, M. Van de Voorde, and K. Sakoda, eds. (2017).
31. X. Fan, J. J. Healy, K. O'Dwyer, and B. M. Hennelly, "Label-free color staining of quantitative phase images of biological cells by simulated Rheinberg illumination," Appl. Opt. **58**, 3104–3114 (2019).